Transient cluster formation in sheared non-Brownian suspensions

Kjetil Thøgersen,[1,*] Marcin Dabrowski,[1,2] and Anders Malthe-Sørenssen[1]
[1]*Department of Physics, University of Oslo, Sem Sælands vei 24, NO-0316 Oslo, Norway*
[2]*Computational Geology Laboratory, Polish Geological Institute–National Research Institute, 53-122 Wroclaw, Poland*
(Received 23 November 2015; published 29 February 2016)

We perform numerical simulations of non-Brownian suspensions in the laminar flow regime to study the scaling behavior of particle clusters and collisions under shear. As the particle fraction approaches the maximum packing fraction, large transient clusters appear in the system. We use methods from percolation theory to discuss the cluster size distribution. We also give a scaling relation for the percolation threshold as well as system size effects through time-dependent fluctuations of this threshold and relate them to system size. System size effects are important close to the maximum packing fraction due to the divergence of the cluster length scale. We then investigate the transient nature of the clusters through characterization of particle collisions and show that collision times exhibit scale-invariant properties. Finally, we show that particle collision times can be modeled as first-passage processes.

DOI: 10.1103/PhysRevE.93.022611

I. INTRODUCTION

Suspensions are ubiquitous in nature. They are important in fields ranging from swimming bacteria [1] and blood flow [2] to lava flows [3,4], debris flows [5], and subsurface contaminant transport [6]. Understanding suspensions is also important for several industrial and technological applications, e.g., for the gas industry [7–9] and in microfluidics [10,11]. Since Einstein's work on the effective viscosity of dilute suspensions [12,13], a large number of studies on particle suspensions have been performed. In 1972, Batchelor and Green extended Einstein's expression of the effective viscosity to second order [14]. The model of Batchelor and Green has since been thoroughly tested experimentally for low-volume fractions ($\phi < 0.1$), and the rheology of dilute suspensions is now well understood [15]. The rheology of dense suspensions is less trivial. Several phenomenological models have been proposed, including the classical Krieger-Dougherty relation, where the viscosity diverges at a maximum packing fraction ϕ_m [16].

A number of studies have related rheology to the interaction between close particle pairs [14,17–22]. Frankel and Acrivos stated that the dominant interaction mode is the compression mode of approaching particles [17] and developed a constitutive relation for effective viscosity for high-particle-volume fractions. Marucci and Denn later pointed out that the tangential mode is dominating, but they also stated that correlated motion over length scales larger than a single particle are important, i.e. the formation of particle clusters [18]. The decrease in the size of the lubrication layer between close particle distances with the shear rate has also been used to demonstrate shear-induced thickening [19]. Several studies have been performed that include interparticle forces. Brady *et al.* have performed several studies on the rheology of suspensions using a short-range repulsive force accounting for particle roughness (e.g., [20,21]). Recent studies have also explained discontinuous shear thickening as a sudden increase in frictional contacts with the shear rate [23]. Studies have also been carried out to unify suspension and granular rheology close to the jamming threshold [24], as well as to understand the rheology of suspensions of nonspherical particles [25].

In 1979, de Gennes proposed a series of conjectures about the microstructure of sheared suspensions [26]. Branched and highly transient particle clusters form in sheared suspensions, but there is a well-defined time-independent size distribution of clusters. He also stated that an infinite cluster would appear as ϕ exceeds a critical threshold value ϕ_c, that the only motion allowed by such clusters would be uniform translations and rotation, and that the divergence of the cluster correlation length follows standard percolation laws. de Gennes' conjectures were recently tested by Gallier *et al.* using numerical simulations based on the fictitious domain method including frictional contacts. They found that most of de Gennes' conjectures hold, but found only a weak correlation between transient spanning clusters and the measured effective viscosity [27].

Suspension microstructure is essential to understand suspension rheology [28,29]. However, while dilute suspensions are fairly well understood, the relation between the microstructure and the rheology of dense suspensions is still lacking, and analytical treatment of microstructure evolution is complicated. The pair distribution function has been used with only limited success to relate rheology and microstructure, even though tensor descriptions of microstructure look more promising [28]. This calls for a different approach to describing the microstructure of suspensions.

From the transient nature of cluster formation as first proposed by de Gennes [26], we expect the maximum cluster size to diverge as the maximum packing fraction is approached. This means that system size effects will be increasingly important for high-particle-volume fractions since the percolation cluster can occur well before the maximum packing fraction [27]. Understanding the transient nature of particle contacts and clustering could therefore provide useful insights into the overall microstructural fluctuations of particle suspensions.

In this work we focus on the transient nature of cluster formation and breakup in suspensions of rigid particles in shear flow, as well as close particle interactions. The methods

*kjetil.thogersen@fys.uio.no

we use are motivated by percolation theory as well as theory of first passages. We define particles to be in contact below a length scale ϵ and the percolation threshold ϵ_c to be the smallest ϵ that results in a particle cluster that spans the system. We establish a scaling relation between percolation and particle fraction, both for the mean percolation threshold $\langle\epsilon_c\rangle$ and for the fluctuations in the percolation threshold $\delta\epsilon_c$, which is system size dependent. As ϕ approaches the maximum packing fraction ϕ_m, the percolation threshold decreases towards 0. For a system of finite size, we then expect transient percolating clusters well before the maximum packing fraction if we define particle contact with a small rim separation $r\epsilon$. We then show that particle contact times are invariant under the choice of ϵ.

In this paper we use a Stokes flow description. Non-Brownian suspensions can often be considered purely viscous materials [15], i.e., the viscosity does not depend on the shear rate. Even though two particles in Stokes flow show reversible dynamics, and their trajectories are symmetric, non-Brownian suspensions show rich dynamics even at zero Reynolds number. Recent studies demonstrate chaotic particle trajectories leading to a threshold of irreversibility related to the growth of the Lyapunov exponent [30]. Chaotic behavior can be demonstrated even for three particles settling under gravity [31], and chaotic rotation has been demonstrated for a single triaxial ellipsoid [32]. This failure of time reversibility shows that chaos is an intrinsic property of slowly sheared suspensions.

The paper is structured as follows: In Sec. II we introduce the finite-element model we use to solve for the particle trajectories. In Sec. III we first introduce a length scale ϵ that defines particle contact, and we then discuss the statistics of cluster formation in the system and give the scaling relations with ϵ based on percolation theory. In Sec. IV we investigate the statistics of particle collisions through the distribution of collision times and introduce a first-passage random walk model that explains several of the observed features of the distribution of collision times. We sum up and conclude in Sec. V.

II. MODEL DESCRIPTION

While numerous numerical techniques have been used to study particle suspensions (e.g., dissipative particle dynamics [33], lattice Boltzmann methods [34], and the LaGrange multiplier fictitious domain method [35]), numerical investigation of particle suspensions has until recently been dominated by studies using Stokesian dynamics simulations [36–38]. In this study we perform direct numerical simulations using the finite-element method. Recent developments allow us to go to large enough strains and particle numbers to perform a statistical analysis. We solve the incompressible Stokes equations. Conservation of mass yields

$$\nabla \cdot \vec{v} = 0, \tag{1}$$

where $\vec{v}$ is the velocity field. Conservation of momentum yields

$$\nabla \cdot \boldsymbol{\sigma} = \vec{0}, \tag{2}$$

where $\boldsymbol{\sigma}$ is the stress tensor, and

$$\boldsymbol{\sigma} = -p\boldsymbol{I} + \boldsymbol{T}, \tag{3}$$

where p is the pressure, $\boldsymbol{I}$ is the identity matrix, and

$$\boldsymbol{T} = \mu(\nabla\vec{v} + (\nabla\vec{v})^T) \tag{4}$$

is the deviatoric stress tensor. We use an adaptive two-dimensional mixed finite-element discretization with the Crouzeix-Raviart seven-node triangular element shape functions for the velocities and discontinuous linear shape functions for the pressure. We use a modified version of MILAMIN for efficient computation in MATLAB [39] and Triangle for meshing [40]. For rigid particles we replace the degrees of freedom associated with the particle boundaries with three degrees of freedom, two translational and one rotational.

In this paper we study the purely hydrodynamic limit, i.e., we use no repulsive forces. In order to achieve this, special care has to be taken with spatial discretization as well as time integration [38]. We use geometrical mesh refinement to ensure that there are at least two elements across the aperture between all close particle pairs at any time during the simulation. In this way we ensure that the velocity field is accurate between close particles. For time integration we use the second-order Runge-Kutta method. We terminate the simulation if particle overlap is detected. For dense suspensions this sets limits on the maximum strains that we can achieve. For statistical measures, it would be beneficial to have one very long run rather than ensemble averaging over multiple shorter ones, but due to computational challenges, the latter is used throughout the paper. Using no repulsive force is especially problematic for large area fractions (two-dimensional volume fraction) where spanning clusters can occur, and particle distances can get infinitesimal, and hence we cannot handle this numerically for arbitrary strains. Still, we present results without any artificial repulsive force up to significant strains for small to moderate area fractions.

An additional strength of the finite-element discretization is that arbitrary domain and particle geometries are trivial to implement, and the velocity and pressure field are solved for at the same time as the particle velocities, which allows for studies of the coupling between fluid and particle motion as well as access to the stress tensor at any position in space and time. However, for simplicity we limit the study to monodisperse disks.

Figure 1 shows a sketch of the system setup. The left and right boundaries are periodic, while the top and bottom boundaries have Dirichlet boundary conditions of opposite velocities, setting up the average shear rate $\dot{\gamma}$. The system is integrated forward in time with a second-order Runge Kutta method with time step $dt = \frac{0.02}{\dot{\gamma}}$. Due to the large computational costs of direct simulations of suspensions using finite elements, the time step should be as large as possible without introducing error terms that are too large. The time step used here is sufficient to conserve the symmetries of two-particle encounters as shown in Fig. 4. We simulate the fully lubricated limit; i.e., the particles always interact through a thin fluid film.

III. CLUSTER STATISTICS

While many models assume a roughness parameter to determine when particles are in contact, we do not have a well-defined contact distance in our system since the particles

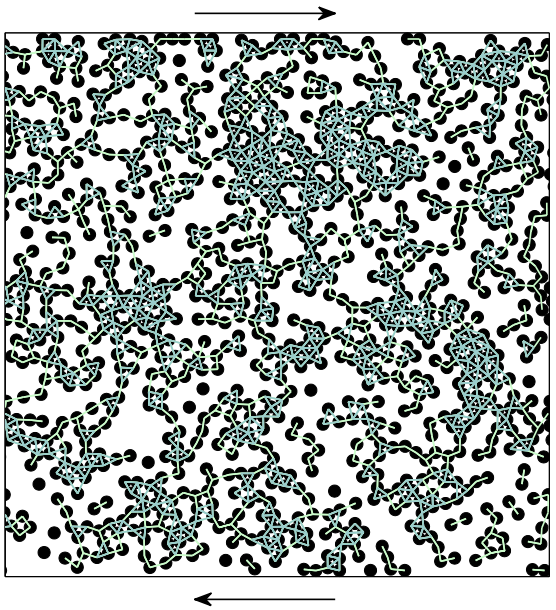

FIG. 1. Sketch of the system setup. The left and right boundaries are periodic, while the top and bottom have velocities in opposite directions to give a background shear rate $\dot{\gamma}$. The particle configuration is a snapshot from a simulation of $N = 1024$ particles at area fraction $\phi = 0.4$, $\epsilon = 1$, $\dot{\gamma}t = 30$. Colored segments are generated from a Delaunay triangulation where only segments shorter than $r(2+\epsilon)$, where r is the particle radius and ϵ is a dimensionless parameter that defines contact, are kept. Here we can see that $\epsilon \geqslant \epsilon_c$, where ϵ_c is the smallest ϵ that gives a spanning cluster in the vertical direction. Segments that form closed triangles have a different shading to highlight the branched cluster structure.

are always separated by a thin fluid film. We define particle clusters using Delaunay triangulation of the particle positions. We define active segments of the triangulation as segments that are shorter than

$$|\vec{\chi}_{ij}| \leqslant r(2+\epsilon), \tag{5}$$

where $|\vec{\chi}_{ij}|$ is the distance between the particle centers, r is the particle radius, and ϵ is a dimensionless distance. The graph of active segments makes up the cluster structure. This definition means that the somewhat arbitrary dimensionless distance ϵ defines whether or not a particle pair is connected. However, we show that several clustering parameters follow classical percolation scaling laws for ϵ, rendering results that are, to a large degree, independent of or insensitive to the choice of ϵ. Figure 1 shows a snapshot of a simulation containing 1024 particles at area fraction $\phi = 0.4$, where we have also highlighted the cluster backbone with triangles where all segments are shorter than $r(2+\epsilon)$ to demonstrate the branched structure and the clusters. In the figure we use $\epsilon = 1$. The clusters in the system are highly transient; they stretch, compress, rotate, and lead to transport of particles in the vertical direction. Particles continuously attach and detach to the clusters, so that the size and lifetime of a cluster are not trivial to define. Still, we show that there is a unique definition of the cluster size distribution if we average in time.

A. Percolation threshold

If the particles were actually in contact, we would have a precise cluster definition. Since this is not the case for slowly sheared incompressible flows (without particle roughness), we need an alternative approach. We define ϵ_c as the lowest threshold at which a spanning cluster occurs. ϵ_c is then a continuous value that goes to 0 if the system is truly percolating, i.e., particles are in direct contact. For an infinite system size, the jamming threshold is expected to coincide with the random close packing fraction [42], which is $\phi_m = 0.82$ for monodisperse disks [41]. Then

$$\lim_{\phi \to \phi_m} \epsilon_c(\phi) = 0. \tag{6}$$

Since $\epsilon_c \to 0$ will not occur in our system (except at maximum packing), the minimum in ϵ_c is the best approximation we can obtain. Figure 2 shows the percolation threshold as a function of time for $N = 1024$ and $\phi = 0.4$. We see that ϵ_c varies by a factor of $\sim$2, indicating the transient nature of the clusters. We also observe that $\langle\epsilon_c\rangle$ is not particularly sensitive to system size effects, while std(ϵ) decreases with the system size as $N^{-1/3}$.

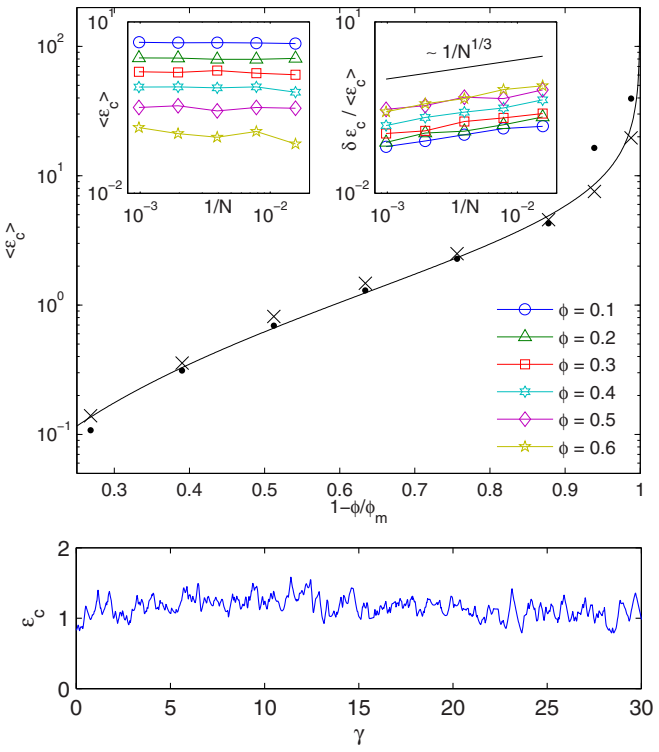

FIG. 2. Top: Dependency of $\langle\epsilon_c\rangle$ on the system size $\frac{1}{N}$ and the area fraction ϕ. $\langle\epsilon_c\rangle$ as a function of the area fraction (crosses, x direction; dots: y-direction). $\langle\epsilon_c\rangle$ scales with $(1-\phi/\phi_m)((\phi/\phi_m)^{-1/2}-1)$ (see text), where $\phi_m = 0.82$ is the maximum random packing fraction [41], in the range of area fractions we have tested. Left inset: System size dependency of $\langle\epsilon_c\rangle$. We find no significant system size effects. Right inset: System size effect of the fluctuations of ϵ_c, here given by the standard deviation. We find that the standard deviation scales with the system size approximately as std(ϵ_c) $\sim N^{-1/3}$. Bottom: Percolation threshold ϵ_c as a function of strain (time) for $N = 1024$ particles at area fraction $\phi = 0.3$.

Using scaling arguments we can predict the behavior of $\langle\epsilon_c\rangle$ with ϕ. At the maximum packing fraction ϕ_m, the system is spanning and ϵ_c goes to 0 according to Eq. (6).[1] This means that for ϕ approaching ϕ_m, we expect that

$$\epsilon_c \sim \left(1 - \frac{\phi}{\phi_m}\right)^{\alpha}, \tag{7}$$

where $\alpha > 0$ is an exponent that could, in principle, depend on ϕ. For small fractions we expect a different scaling behavior. In very dilute systems, we can assume that the configuration does not depend on the particle radius, so that changing ϕ is equivalent to reducing r for all particles. Then

$$r(2 + \epsilon_c) \approx \text{constant} \tag{8}$$

as r is reduced, and the constant is expected to be of the order of $L/\sqrt{N}$, where L is the length of the simulation box. We are searching for a relation that has the correct divergence of ϕ in the dilute limit and is still well behaved in the dense limit. Using the relation $r \sim \phi^{\frac{1}{2}}$, ϵ_c is well approximated through

$$\epsilon_c \sim \left(\left(\frac{\phi}{\phi_m}\right)^{-\frac{1}{2}} - 1\right), \tag{9}$$

which is positive for $\phi \in [0,\phi_m]$. One scaling relation that gives the expected behavior in both limits is

$$\epsilon_c \approx C\left(1 - \frac{\phi}{\phi_m}\right)^{\alpha}\left(\left(\frac{\phi}{\phi_m}\right)^{-\frac{1}{2}} - 1\right), \tag{10}$$

where C is a constant. Figure 2 shows $\langle\epsilon_c\rangle$ as a function of ϕ. We obtain a good fit using $\alpha = 1$ and $C = 3$.

1. Cluster size distribution

We define the cluster size s as the number of particles that form a connected structure. We then measure the cluster number density $n(s,\epsilon)$ for different values of ϵ. The cluster size distribution is highly dependent on the choice of the threshold parameter ϵ. This is expected if we look at the system as a percolation system where we have a percolation threshold $\epsilon_c(\phi)$ that depends on the area fraction ϕ. Figure 3 shows the cluster number density for 1024 particles at $\phi = 0.3$ for various ϵ's, where the largest clusters are removed because they could, in principle, be spanning. As ϵ approaches the percolation threshold ϵ_c, the cutoff in cluster size diverges and we get a power-law distribution of cluster sizes; i.e., all clusters of all sizes exist. We obtain a decent collapse of the data using the universal percolation scaling exponent $\sigma = 36/91$, which describes the cutoff in the cluster size distribution as ϵ_c is approached, and $\tau = 187/91$, which is the power-law exponent of the cluster size distribution at the percolation threshold [43]. However, even longer time series are needed to obtain enough statistics to reach a firm conclusion on this matter.

[1]Note that there can be subtle differences between the isotropic maximum packing fraction and jamming when the system is anisotropic, and we do observe minor systematic differences in the percolation threshold in the x and y directions.

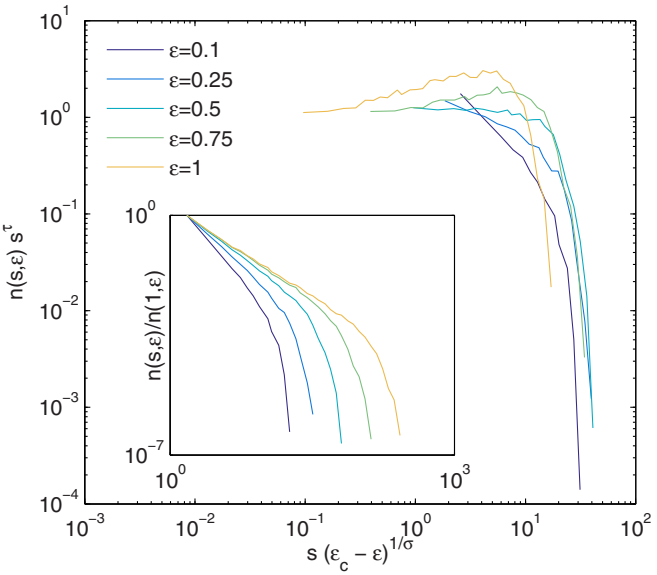

FIG. 3. Cluster number density scaled with traditional percolation parameters. $N = 1024$, $\phi = 0.3$. Scaled with universal percolation exponents $\tau = \frac{187}{91}$, the exponent of the power-law distribution at the measured percolation threshold $\epsilon_c = 1.34$, and $\sigma = \frac{36}{91}$, which describes how the cutoff in cluster size diverges as the threshold is increased towards the percolation threshold. Inset: Unscaled distributions. All data are equilibrated for $\gamma = 20$.

Using the combination of the universal scaling exponents τ and σ for the cluster size distribution as well as the scaling relation between $\langle\epsilon_c\rangle$ and ϕ, we can uniquely determine the cluster size distribution given ϕ and ϵ. The fluctuations are also well described through $\delta\epsilon_c \sim N^{-\frac{1}{3}}$. With this result established, we now turn to the particle collisions.

IV. COLLISION STATISTICS

Since we are dealing with an incompressible fluid in the laminar regime and smooth particle surfaces, the particles are not touching, they are only interacting through the fluid phase. This means that we need to define what a collision is based on a length scale that is not related to any physical quantities. However, as we will discuss in this section, many results will not be sensitive to this choice.

A. Collision trajectories

In the previous section we have defined a length scale that we continue to use. We define two particles to be colliding when they are within the distance $|\vec{\chi}_{ij}| \leqslant r(2 + \epsilon)$. Figure 4 shows the collision between two particles in simple shear, when they are the only particles present in the system. The black lines shows trajectories of the first particle in the reference frame of the second particle. The blue region is inaccessible since the particles have the same radius r. The green region is the region defining the collision between the two particles. Note that there are two types of trajectories: open trajectories and losed trajectories, first described by Batchelor and Green in 1972 [44], which will stay in contact indefinitely

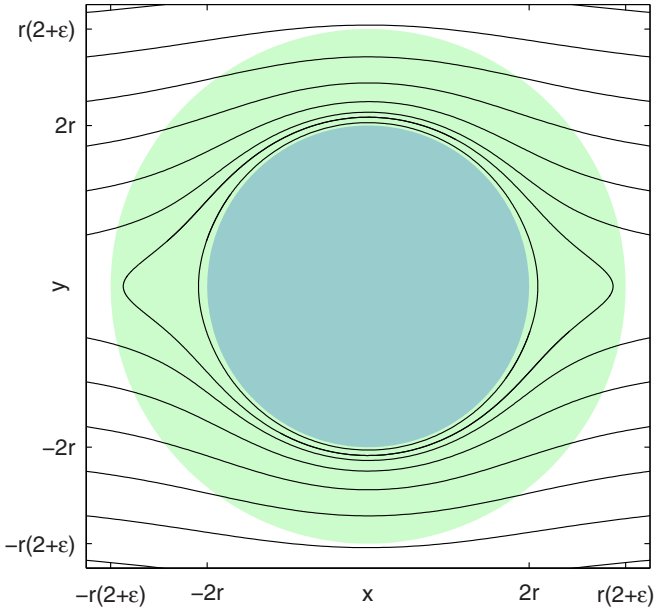

FIG. 4. Trajectory of two-particle collisions. The first particle position is used as a reference frame. In incompressible flow, particles will not actually touch. The blue circle shows the inaccessible region of radius $2r$, while the outer green circle shows the cutoff ϵ used to define collisions. Note the existence of closed trajectories. The figure was generated from simulations of two particles in simple shear with $dt = \frac{0.02}{\dot{\gamma}}$ with a second-order Runge-Kutta integrator and a resolution similar to that in the rest of the simulations presented in this paper.

as long as no additional particles are present that could disturb the trajectory.

The collisions in suspensions are more complex due to the interaction between more than two particles. Data from a simulation of $N = 1024$ particles at area fraction $\phi = 0.1$ are shown in Fig. 5. (Trajectories for larger ϕ's are shown in Appendix A.) From the figure one can clearly distinguish two regimes: one for short-duration collisions and one for long-duration collisions. Short-duration collisions follow open trajectories similar to those demonstrated in Fig. 4, with some deviation due to simultaneous interaction with other particles. In addition, we observe trajectories similar to swapping trajectories that were described by Zurita-Gotor *et al.* [45] (we find that these trajectories are quite rare). It is, however, not clear whether these trajectories occur due to the swapping mechanism, which is related to boundary effects, or if they originate from interactions between more than two particles.

The long-duration collisions follow trajectories more similar to the closed trajectories in Fig. 4. We interpret the long-duration collisions as particles that are pushed into closed orbits by random interaction with multiple particles and then back to open trajectories before they escape. This is visible in the top-right panel in Fig. 5, where one can see that the trajectories complete several loops before they escape.

To quantify the trajectory shape, we introduce the excursion profile, which is a common measure in first-passage random walks [46,47]. We reduce the problem to one dimension by considering only the radial distance d_{ij} and velocity $v_{r,ij}$ between colliding particles. Collisions that are ongoing at the start or end of the simulations are not counted. A few examples of such excursions are shown in the bottom two panels in Fig. 5. The short collisions exhibit close-to-parabolic shapes, while the longer collisions fluctuate in d_{ij}. To quantify the shape of the excursions, we scale the time axis of the individual excursions by the excursion time, $\Delta\gamma$, and average. Figure 6 shows the mean excursion shape for various ϕ and ϵ values scaled by the maximum value of the curves. As expected from the symmetry of Stokes equations, the average excursions are symmetric in time. A decreasing ϵ pushes the shape from parabolic towards semicircular, which is related to the hydrodynamic forces of very close particles. An increasing ϕ has the same effect. However, the effects are not particularly large over the range we have tested ($\epsilon \in [0.1,2]$ and $\phi \in [0.1,0.4]$).

B. Collision times

Another quantity of interest is the distribution of collision times, i.e., how long particle contacts last. Figure 7 shows the distribution of contact times for various ϵ and ϕ values. As previously, collisions that are ongoing at the start or end of the simulations are not counted. The distribution of collision times has the surprising feature that it is scale invariant, i.e., independent of ϵ for a wide range of ϵ values tested. Also, it is not sensitive to system size and only weakly dependent on the particle area fraction ϕ. The short collision times are dominated by open trajectories where the probability density scales as $\Delta\gamma$, with the most likely collision time of order $\Delta\gamma \approx 1$. Short collision times are well described by the hydrodynamic interaction between members of an isolated particle pair. Long collision times, however, exhibit a different scaling; we observe a scaling exponent $\approx\Delta\gamma^{-3}$.

While Stokes equations are in principle reversible, it has been shown that slowly sheared suspensions exhibit chaotic behavior [48]. Stochastic-like behavior is possible even in deterministic systems, if they are chaotic [49]. This concept has been been discussed in light of shear-induced self-diffusion in suspensions, which occurs even without the presence of Brownian motion [48]. Here, we are interested in the relative motion of close particle pairs, so we use the same concept and assume that interactions with additional particles can be modeled as a series of statistically independent events. This allows us to approximate the motion of close particle pairs as random walks.

In an attempt to explain the scaling behavior in Fig. 7, we turn to the theory of first passages. It follows from straightforward scaling arguments that the first-passage distribution of a random walk is scale invariant under the condition that the standard deviation of the velocity over the mean value of the velocity is kept constant, i.e., $\delta v/\langle v\rangle = \text{constant}$. This is consistent with the standard deviation and mean velocity measured for collisions in our data. The results are shown in Fig. 8, where we see that equal ϕ's have equal ratios $\delta v_r/\langle v_r\rangle$.

The first-passage time distribution of a random walk is a power-law distribution with exponent $\beta = -\frac{3}{2}$ [50], which does not match the long-time limit observed in our data. One possible explanation for this discrepancy is long-time correlations of the collision velocities. We would then expect a transition from $\beta = -3$ to $\beta = -\frac{3}{2}$ in the very-long-time limit. The reason we did not see this is because our time series

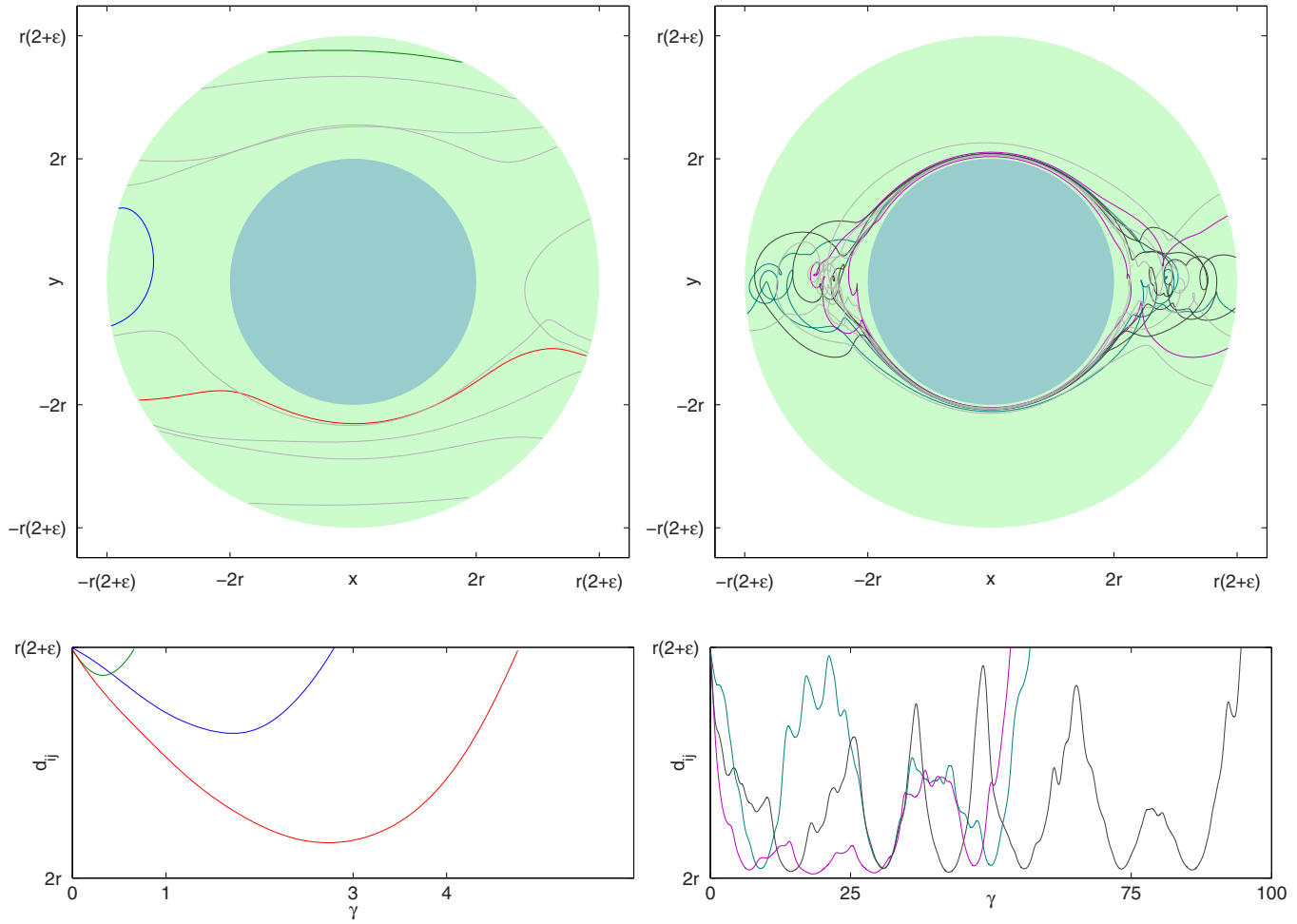

FIG. 5. Example collisions with $\epsilon = 2$ from a simulation of $N = 1024$ particles at area fraction $\phi = 0.1$ in simple shear demonstrating two collision regimes. Top left: Examples of collisions with collision time $\Delta\gamma \leqslant 5$. Top right: Collisions with collision time $\Delta\gamma \geqslant 50$. Bottom: Distance between the two particles as a function of γ. The line colors correspond to the line colors (darker lines) in the top figures.

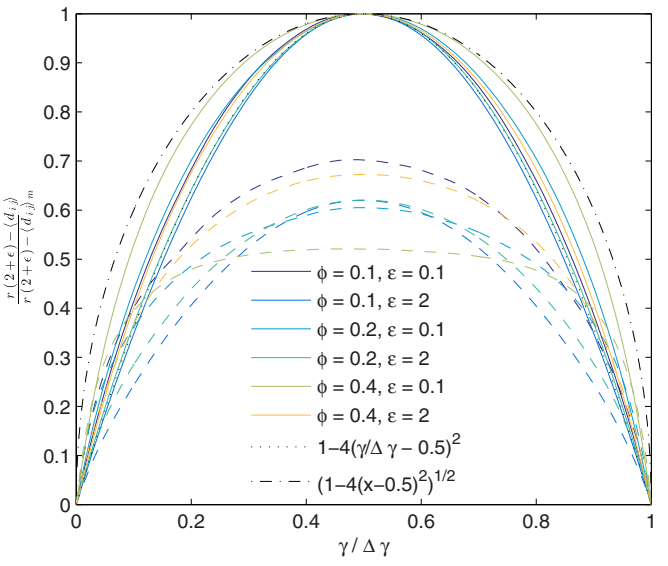

FIG. 6. Average excursion $\langle d_{ij}\rangle$ scaled by the minimum excursion $\langle d_{ij}\rangle_m$. Dashed lines show the standard deviation. A decrease in ϵ pushed the mean excursion from fairly parabolic towards semicircular. All data are from simulations of $N = 1024$ particles.

are not long enough. Even though collisions that long are very unlikely, the scaling behavior for long collision times is important to determine whether or not the mean collision time diverges because the first moment of a power-law distribution diverges for $\beta > -2$.

C. First-passage random walk model

We attempt to model the collision time distribution using correlated random walks. The first thing we need to do is to parametrize the parameters that we need to input to the random walk. They are the mean radial velocity during a collision and the standard deviation, as well as the self-correlation of each walk. For the self-correlation we use the power spectrum because we use the same power spectrum to generate random walks. We perform a discrete Fourier transform of v_r for all collisions that last longer than $\Delta\gamma = 50$. This is because the short collisions are not long enough to get reliable frequency spectra. The insets in Fig. 9 show δv_r, $\langle v_r\rangle$, and the frequency spectrum $P_{v_r}(1/\gamma)$ for a single run with $N = 1024$, $\phi = 0.1$, and $\epsilon = 2$, as well as the fits used as inputs for the random walk model. δv_r and $\langle v_r\rangle$ show the correlations on the time scale of order $\delta\gamma \sim 20$. The frequency spectrum shows power-law

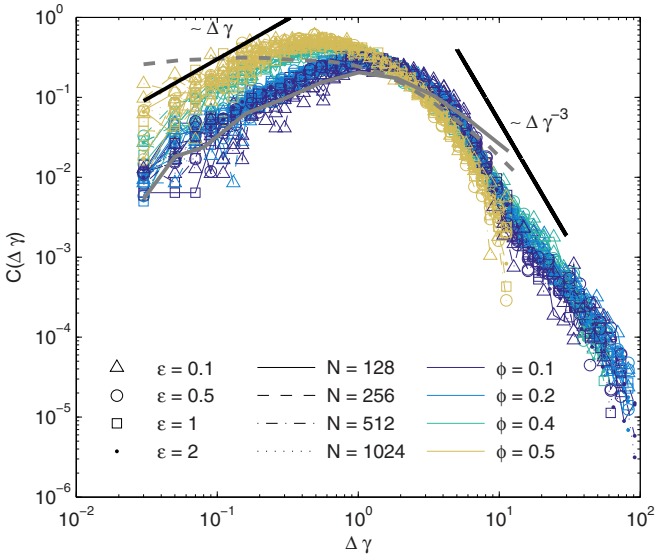

FIG. 7. Probability density of collision times $C(\Delta\gamma)$. The curve is invariant under ϵ and N but has a weak dependence on ϕ. Long collision times scale as $\Delta\gamma^{-3}$, but we expect a transition to $\Delta\gamma^{-3/2}$ for even longer times (see text and Fig. 9). Thick gray lines show results from two particles with $\epsilon = 1$, where the initial relative positions show radial symmetry (dashed gray line) and a uniform distribution in y at $-r(2+\epsilon)$ (solid gray line).

noise at high frequencies and a transition to white noise at low frequencies.

We construct our random walk in Fourier space that satisfies the measured power spectrum. Each collision velocity v_r follows a power spectrum made from uniform random weights scaled with $P_{v_r}(1/\gamma)$. $v_r(\gamma)$ is then obtained from an inverse discrete Fourier transform. We then multiply by the measured standard deviation and add the mean value that we observed. The resulting collision time distribution C is plotted in Fig. 9. The correspondence with our data from finite-element simulations is very good, and the simplified model also predicts a crossover from $\beta = -3$ to $\beta = -\frac{3}{2}$ at very long times. This transition from pink noise at high frequencies to white noise at low frequencies is responsible for the power-law

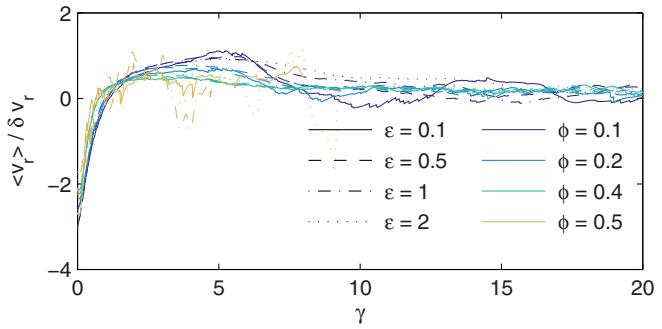

FIG. 8. Ratio between the standard deviation δv_r and the mean radial velocity $\langle v_r \rangle$ for colliding particles. Only particles within the distance $r(2+\epsilon)$ contribute to the curves. Equal ϕ (equal colors) collapse onto the same lines for different ϵ's, consistent with scale invariance of the return time of random walks.

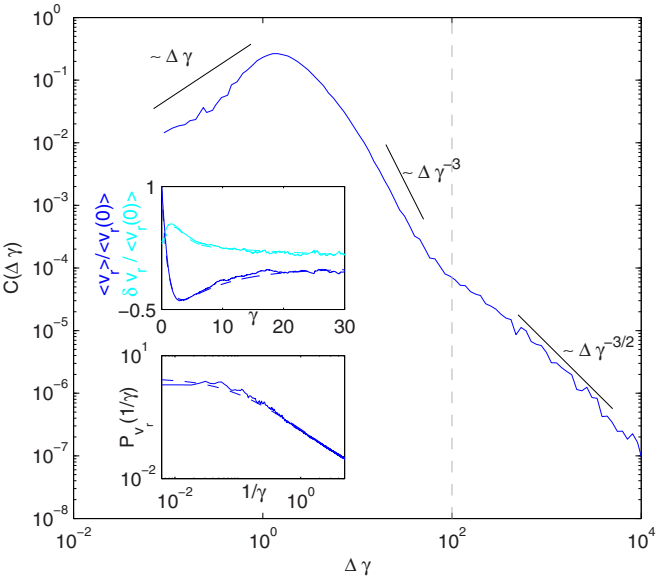

FIG. 9. First-passage probability density for the random walk model with data for $N = 1024$, $\phi = 0.1$, and $\epsilon = 2$. The features from the finite-element data are recovered, and a $\beta = -\frac{3}{2}$ scaling is found for large $\Delta\gamma$. The gray line shows the boundaries in Fig. 7. Top inset: Mean and standard deviation of v_r from finite-element data. Dashed lines show the parameterized curves that are used as inputs for the random walk. Bottom inset: Frequency spectrum of v_r from finite-element data where we have subtracted $\langle v_r \rangle$. Only data from collisions with $\Delta\gamma > 50$ are used. The dashed line shows the parameterized curve used in the random walk model. Note the transition from pink $(1/f^a)$ noise at high frequencies to white noise (constant) at low frequencies.

behavior with $\beta = -\frac{3}{2}$ in $C(\Delta\gamma)$ for $\Delta\gamma \gtrsim 10^2$. The good correspondence between the collision time probability density and the return time of the correlated random walk suggests that our interpretation of the collisions as particles that are pushed into what would, in the two-particle case, be closed orbits, and are then subjected to random interactions with additional particles in the suspensions, is justified. Details of the effect of P_{v_r}, δv_r, and $\langle v_r \rangle$ are discussed in Appendix B.

V. DISCUSSION AND CONCLUSION

In this paper we have introduced a two-dimensional finite-element model to study particle suspensions in simple shear at zero Reynolds number. We use geometrical mesh refinement in the regions between close particles to assure that lubrication forces are modeled accurately. This allows us to avoid the use of repulsive forces that are commonly implemented to avoid particle overlaps. This does set constraints on the γ we can reach for high-particle-area fractions, but we have reached γ values large enough to perform a statistical analysis when combined with ensemble averaging.

The particles form transient clusters that rotate and transport particles in the vertical direction. To study the cluster statistics we have introduced a dimensionless contact length ϵ and investigated how particle collision statistics depend on this length. The cluster number density follows classical percolation theory and scales with the universal scaling exponents

τ and σ. While the percolation threshold fluctuates in time, with the fluctuations scaling with the system size as $N^{-\frac{1}{3}}$, the time-averaged cluster number density is well defined.

Even though de Gennes proposed that transient spanning clusters are directly related to an increase in the effective viscosity, a recent study by Gallier *et al.* [27] finds that, although spanning clusters can support more stress, the correlation between the effective viscosity and the occurrence of transient spanning clusters is weak. However, the relation between effective viscosity and cluster formation in suspensions is still an interesting research question for future studies.

Two particles in simple shear exhibit two types of collision trajectories: open and closed trajectories. For particle collisions where many particles are present and can change the trajectories of a particle pair, this distinction is still visible. Short collisions are similar to open collision trajectories involving only two particles, while we interpret long collisions as particles pushed into what would, in the two-particle case, be closed trajectories. The trajectories are then subject to random interactions with other particles, until they are pushed out of the closed trajectory. This interpretation is supported by the close resemblance between the collision time probability density and the return time of a correlated random walk. Using $\langle v_r \rangle$ and δv_r as well as the power spectrum of each collision trajectory, we have reproduced the collision time probability density. We also predict that the long-time behavior scales as a power law with exponent $\beta = -\frac{3}{2}$, but we have not reached strains large enough to confirm this prediction. $\beta = -\frac{3}{2}$ in the long-time limit indicates that the mean collision time diverges since the first moment of a power-law distribution with exponent $\beta > -2$ diverges. Due to the conservation of the ratio $\delta v_r / \langle v_r \rangle$ with changing ϵ, the distribution of the collision time is scale invariant. This is again due to the self-affine properties of v_r, which are visible in the power spectrum P_{v_r}.

Our results on the collision time probability density highlight some of the challenges we face with regard to long-time series using finite-element simulations of particle suspensions. The interpretation of contacts as first-passage processes implies that we are quite likely to find very close particle pairs in sheared suspensions. The probability of finding such pairs would scale with the total number of contacts, i.e., N and ϕ, as well as the total strain γ. Close particle pairs are difficult to treat numerically due to the large variation in element size and the singularity of the zero spacing between particles; this puts severe constraints on the likelihood of running large systems to large strains. To overcome this difficulty, approaches such as upscaling of the lubrication layer between close particles and short-range repulsive forces are necessary.

Several studies have been performed using repulsive forces motivated by friction, electrostatic repulsion, or van der Waals forces (see, e.g., [20], [21], [23], and [29]). Even short-range repulsive forces will break the symmetry of the two-particle interaction in Fig. 4. We do not expect short-range repulsive forces to change the short collision trajectories significantly, but the long collisions will be altered, and if the repulsive force is large enough, closed trajectories will cease to exist.

An interesting question is whether simple random walk models can be used to predict the transient properties of the cluster size distribution. Given the probability density of particle collision times, one would imagine that combining it with a collision rate could lead to predictions of the cluster size distribution using a purely statistical approach. However, we leave this open for possible future investigations. Understanding the microstructure of particle suspensions and, in particular, the transient nature of close particle contacts is an important step towards understanding the relation between suspension microstructure and effective properties, including fluctuations. In particular, close to the maximum packing fraction, the fluctuations in the percolation threshold show that transient percolation clusters appear.

ACKNOWLEDGMENTS

We acknowledge support from the Norwegian High Performance Computing (NOTUR) network through the grant of machine access. K.T. acknowledges support from VISTA, a basic research program funded by Statoil, conducted in close collaboration with The Norwegian Academy of Science and Letters.

APPENDIX A: RELATIVE PARTICLE TRAJECTORIES FOR $\phi = 0.3$ AND $\phi = 0.4$

To supply the trajectories plotted in Fig. 5, we give a few examples of relative particle trajectories for $\phi = 0.3$ and $\phi = 0.4$ in Fig. 10. While the concept of open and closed trajectories still applies, the trajectories for large ϕ are more complex than what we observe for $\phi = 0.1$.

APPENDIX B: DETAILS OF THE RANDOM WALK MODEL

In this section we give the details of the random walk model used in the discussion of the collision times. The parameterized

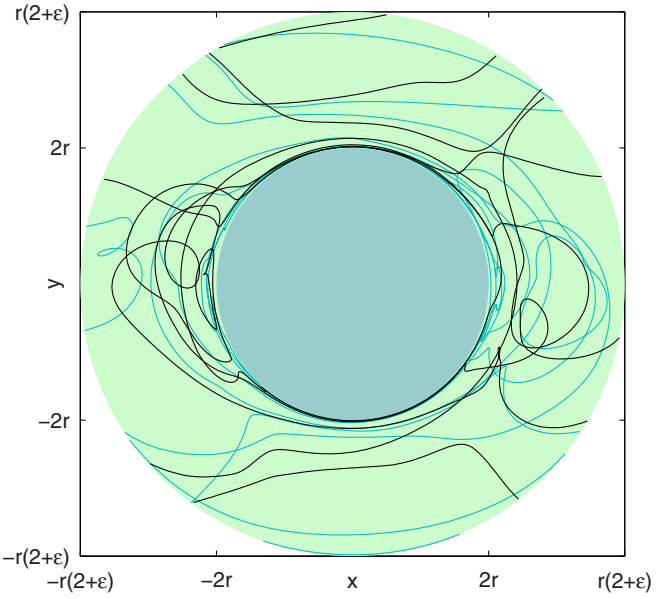

FIG. 10. Examples of relative particle trajectories for $N = 1024$ at $\phi = 0.3$ (cyan lines) and $\phi = 0.4$ (black lines).

curves we use at inputs are

$$P_{v_r}(1/\gamma) \sim \frac{1}{\left(1+\frac{b}{\gamma}\right)^a}, \tag{B1}$$

$$\frac{\langle v_r\rangle}{\langle v_r(0)\rangle} = \frac{5}{3}e^{-\gamma/c} - \frac{2}{3}e^{-\gamma/d}, \tag{B2}$$

and

$$\frac{\delta v_r}{\langle v_r(0)\rangle} = \frac{2}{5}\gamma^2 e^{-\gamma} + \frac{1}{4}e^{-\gamma/40} + \frac{1}{20}, \tag{B3}$$

where we have used $a = 1.1$, $b = 12.5$, $c = 1$, and $d = 8$ in the model in the text. The random walk is constructed using uniform random weights scaled with P_{v_r}. In addition, we use cutoff frequencies $1/\gamma > 5$. We then perform an inverse discrete Fourier transform, scale it to get the correct standard deviation $\frac{\delta v_r}{\langle v_r(0)\rangle}$, and add $\frac{\langle v_r\rangle}{\langle v_r(0)\rangle}$ to get v_r.

Figure 11 shows how a, b, c, and d control the shape of $C(\Delta\gamma)$, where we have performed a series of random walks and measured $C(\Delta\gamma)$. a and b control the behavior at long times, while c and d control the short-time behavior. a controls the fractal dimension of the walk at high frequencies, while b controls the crossover from a self-affine walk to white noise. c shifts the maximum point of $C(\Delta\gamma)$, while d controls the shape of the peak. It is the combination of these parameters that makes up Fig. 9.

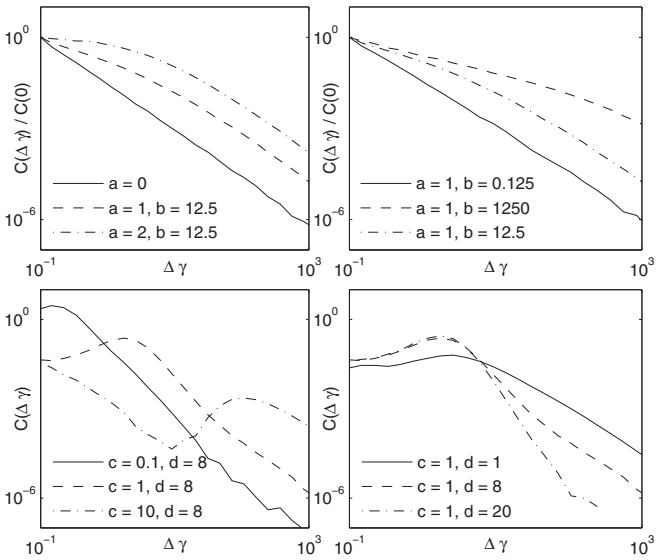

FIG. 11. Measurements of the return time distribution for random walks following Eqs. (B1), (B2), and (B3). Top left: Effect of a on the return time distribution $C(\Delta\gamma)$. $\langle v_r\rangle = 0$, δv_r = constant. Top right: Effect of b on the return time distribution $C(\Delta\gamma)$. $\langle v_r\rangle = 0$, δv_r = constant. Bottom left: Effect of c on the return time distribution $C(\Delta\gamma)$. $a = 1$, $b = 12.5$, $\frac{\delta v_r}{\langle v_r\rangle} = \frac{2}{5}$. Bottom right: Effect of d on the return time distribution $C(\Delta\gamma)$. $a = 1$, $b = 12.5$, $\frac{\delta v_r}{\langle v_r\rangle} = \frac{2}{5}$.

[1] E. Lushi, H. Wioland, and R. E. Goldstein, Proc. Natl. Acad. Sci. USA **111**, 9733 (2014).
[2] J. B. Freund, Annu. Rev. Fluid Mech. **46**, 67 (2014).
[3] P. Yamato, R. Tartese, T. Duretz, and D. A. May, Tectonophysics **526**, 97 (2012).
[4] A. F. Glazner, Geology **42**, 935 (2014).
[5] P. Coussot and M. Meunier, Earth-Sci. Rev. **40**, 209 (1996).
[6] J. F. McCarthy and J. M. Zachara, Environ. Sci. Technol. **23**, 496 (1989).
[7] P. Meakin, H. Huang, A. Malthe-Sørenssen, and K. Thøgersen, Environ. Geosci. **20**, 151 (2013).
[8] N. Patankar, D. Joseph, J. Wang, R. Barree, M. Conway, and M. Asadi, Int. J. Multiphase Flow **28**, 1269 (2002).
[9] V. A. Kuzkin, A. M. Krivtsov, and A. M. Linkov, J. Min. Sci. **50**, 1 (2014).
[10] G. M. Whitesides, Nature **442**, 368 (2006).
[11] X. Xuan, J. Zhu, and C. Church, Microfluid. Nanofluid. **9**, 1 (2010).
[12] A. Einstein, Ann. Phys. **14**, 229 (2005).
[13] A. Einstein, Ann. Phys. **339**, 591 (1911).
[14] G. Batchelor and J. Green, J. Fluid Mech. **56**, 401 (1972).
[15] G. Ovarlez, F. Bertrand, and S. Rodts, J. Rheol. **50**, 259 (2006).
[16] I. M. Krieger and T. J. Dougherty, Trans. Soc. Rheol. **3**, 137 (1959).
[17] N. Frankel and A. Acrivos, Chem. Eng. Sci. **22**, 847 (1967).
[18] G. Marrucci and M. Denn, Rheol. Acta **24**, 317 (1985).
[19] L. Y. Iskakova and A. Y. Zubarev, Phys. Rev. E **88**, 032303 (2013).
[20] A. Sierou and J. Brady, J. Rheol. **46**, 1031 (2002).
[21] J. F. Brady and J. F. Morris, J. Fluid Mech. **348**, 103 (1997).
[22] P. Mills and P. Snabre, Eur. Phys. J. E **30**, 309 (2009).
[23] R. Seto, R. Mari, J. F. Morris, and M. M. Denn, Phys. Rev. Lett. **111**, 218301 (2013).
[24] F. Boyer, É. Guazzelli, and O. Pouliquen, Phys. Rev. Lett. **107**, 188301 (2011).
[25] S. Mueller, E. Llewellin, and H. Mader, in Proc. R. Soc. London Ser. A **466**(2116), 1201 (2009).
[26] P. De Gennes, J. Physique **40**, 783 (1979).
[27] S. Gallier, E. Lemaire, F. Peters, and L. Lobry, Phys. Rev. E **92**, 020301 (2015).
[28] J. J. Stickel and R. L. Powell, Annu. Rev. Fluid Mech. **37**, 129 (2005).
[29] J. F. Morris, Rheol. Acta **48**, 909 (2009).
[30] D. Pine, J. Gollub, J. Brady, and A. Leshansky, Nature **438**, 997 (2005).
[31] I. M. Jánosi, T. Tél, D. E. Wolf, and J. A. C. Gallas, Phys. Rev. E **56**, 2858 (1997).
[32] A. Yarin, O. Gottlieb, and I. Roisman, J. Fluid Mech. **340**, 83 (1997).
[33] P. Hoogerbrugge and J. Koelman, Europhys. Lett. **19**, 155 (1992).
[34] A. Ladd and R. Verberg, J. Stat. Phys. **104**, 1191 (2001).

[35] R. Glowinski, T.-W. Pan, T. I. Hesla, and D. D. Joseph, Int. J. Multiphase Flow **25**, 755 (1999).
[36] J. F. Brady and G. Bossis, Annu. Rev. Fluid Mech. **20**, 111 (1988).
[37] J. F. Brady and G. Bossis, J. Fluid Mech. **155**, 105 (1985).
[38] M. L. Ekiel-Jeżewska, T. Gubiec, and P. Szymczak, Phys. Fluids **20**, 063102 (2008).
[39] M. Dabrowski, M. Krotkiewski, and D. Schmid, Geochem. Geophys. Geosyst. **9**, Q04030 (2008).
[40] J. R. Shewchuk, in *Applied Computational Geometry Towards Geometric Engineering* (Springer, Berlin, 1996), pp. 203–222.
[41] J. G. Berryman, Phys. Rev. A **27**, 1053 (1983).
[42] C. S. O'Hern, L. E. Silbert, A. J. Liu, and S. R. Nagel, Phys. Rev. E **68**, 011306 (2003).
[43] D. Stauffer and A. Aharony, *Introduction to Percolation Theory* (CRC Press, Boca Raton, FL, 1994).
[44] G. Batchelor and J.-T. Green, J. Fluid Mech. **56**, 375 (1972).
[45] M. Zurita-Gotor, J. Bławzdziewicz, and E. Wajnryb, J. Fluid Mech. **592**, 447 (2007).
[46] A. Baldassarri, F. Colaiori, and C. Castellano, Phys. Rev. Lett. **90**, 060601 (2003).
[47] F. Colaiori, A. Baldassarri, and C. Castellano, Phys. Rev. E **69**, 041105 (2004).
[48] G. Drazer, J. Koplik, B. Khusid, and A. Acrivos, J. Fluid Mech. **460**, 307 (2002).
[49] P. Gaspard, *Chaos, Scattering and Statistical Mechanics*, Vol. 9 (Cambridge University Press, Cambridge, UK, 2005).
[50] S. Redner, *A Guide to First-Passage Processes* (Cambridge University Press, Cambridge, UK, 2001).